POLITECNICO DI TORINO
Repository ISTITUZIONALE

SKA-Low Prototypes Deployed in Australia:
Synoptic of the UAV-Based Experimental Results

(Article begins on next page)

09 August 2022

SKA-low Prototypes Deployed in Australia: Synoptic of the UAV-based Experimental Results

Fabio Paonessa, Lorenzo Ciorba, Giuseppe Virone, Pietro Bolli, Alessio Magro, Andrew McPhail, Dave Minchin, and Raunaq Bhushan

Abstract – As the Square Kilometre Array progresses toward the construction phase, the first prototypes of the low-frequency instrument have been deployed in Australia. To support such a crucial phase, a measurement campaign took place in the Murchison Radio-astronomy Observatory area in order to validate the electromagnetic models of the arrays by characterizing the embedded-element patterns and the array beams. This letter shows the large amount of campaign results in a comprehensive and readable way. Such a synoptic visualization allows for a direct evaluation of the complete dataset.

1. Introduction

The future Square Kilometre Array (SKA) [1] radio telescope is approaching the final stage of its development. Within the bridging phase of the low-frequency instrument (SKA-low) [2], which will operate from 50 MHz to 350 MHz, two stations have been built in the Murchison Radio-astronomy Observatory (MRO) area in Western Australia. Both the stations share an aperiodic (random) array layout of 256 dual-polarized antennas mounted on a ground plane with a diameter of about 40 m. The Aperture Array Verification System 2.0 (AAVS2.0) station is composed of log-periodic SKALA4.1-AL antennas [3], whereas the Engineering Development Array 2 (EDA2) [4] station is composed of bow-tie antennas already used in the Murchison Widefield Array (MWA) [5].

The accuracy of the electromagnetic models is a critical aspect for such advanced instruments. The embedded element patterns (EEPs) can present significant distortions with respect to the behavior of a stand-alone antenna [6]. In June 2019, a measurement campaign was carried out at MRO with the main purpose of validating the electromagnetic models of both arrays through an experimental measurement of the EEPs and the digitally beam-formed array patterns exploiting a radio-frequency test source mounted on a small unmanned aircraft. The measurements directly involved research institutions from Italy, Australia and Malta. Before this campaign, the Italian team conducted several activities on low frequency aperture arrays, including the instrumental calibration [7-9] and near-field verification strategies [10, 11]. This letter shows the relevant results of the MRO campaign extending the

contribution of URSI GASS 2020 [12]. In particular, a figure-of-merit for the agreement between simulated and measured pattern has been adopted in order to obtain a direct synoptic visualization of the complete dataset. This data processing and organization is relevant for the future development of station verification strategies in the framework of SKA-low and other aperture arrays. Moreover, the EEPs already shown in [12] have been updated after a further data analysis that identified an issue in the time-synchronization between the acquired data.

2. Experimental Setup

When the MRO campaign was carried out, only 48 antennas out of 256 were deployed in 3 clusters of 16 elements for AAVS2.0, for this reason its name was AAVS1.5 [13]. EDA2 was fully deployed but only 48 antennas where connected to the receiver. The disconnected elements are included in the EDA2 model. The arrays shared nearly the same geometrical layout. In particular, the layout of AAVS1.5 (illustration in Figure 1) is slightly enlarged with respect to EDA2 to accommodate the larger footprint of the elements. The resulting station diameter is 40 m for AAVS1.5 and 35 m for EDA2.

The complex voltages have been acquired for each element (both polarizations). The channel bandwidth of 0.78125 MHz has been narrowed by a factor of 128 (digital filtering) with an oversampling factor of 32/27. This setting produces a data rate of about 27 Mbyte/min for each cluster of 16 antennas, both polarizations. The length of time series was about 3 minutes for each field cut. Although a relatively small subset of antennas was deployed when the campaign took place, more than 10 GB of data have been collected in two days, corresponding to 14 flights.

The measurements at MRO have been carried out by using the Unmanned Aerial Vehicle (UAV) system already adopted in [14, 15]. A small multicopter equipped with a tunable RF generator and a tunable dipole antenna operated as a flying test source, while a Real Time Kinematic (RTK) differential GPS provided centimeter-level accurate position data. The displacement of a few centimeters between the phase centers of the GPS and test source antennas does not affect the amplitude measurements reported in this work.

The measurements have been performed at the frequencies of 50 MHz, 70 MHz, 110 MHz, 160 MHz, 230 MHz and 320 MHz. They consisted in linear scans passing through the array center at constant height to characterize the radiation patterns with an angular coverage of ±45° from zenith [16]. Such a flying height was originally programmed to 160 m for all the measurements, but due to adverse wind conditions some

measurements have been executed at 120 m. It should be pointed out that the flight paths do not lie in the *E*-/*H*-plane of all the antennas; however, both measurements and simulations are computed on the measured path.

Rigorously speaking, the far-field condition is satisfied at cluster level (see Figure 1) only up to 120 MHz. Nevertheless, at higher frequency the agreement between measurements and simulations (see next section) is still satisfactory. This is an indirect confirmation that the radius-of-influence is not very large and certainly below the subarray diameter. The procedure in [10] could be adopted to better quantify the near-field effects.

3. Results

Figure 2 shows the normalized EEPs of two antennas of AAVS1.5 (#0 and #2 of cluster #0) at two different frequencies (70 MHz and 320 MHz). Element #0 is located at the edge of the cluster whereas #2 is closer to other adjacent antennas. Figure 3 shows the results for the corresponding elements in the EDA2 station. As previously mentioned, both the arrays share the same layout. With respect to [12], a further data analysis allowed to identify an issue in the timestamp assignation. In particular, a time-shift of about 1 s has been determined between the UAV data and the measured RF signal at the receiver level by aligning fast modulation features produced by wind gusts in small portions of the flight. The already good agreement between the original EEPs (blue curves) and the simulations (red curves) has been further improved applying the time-shift correction to the measured signals. The re-elaborated EEPs (green curves) show both a better agreement and a smaller ripple. The logarithmic difference (see (6) of [17]) has been adopted as figure-of-merit for the discrepancy between simulated and measured pattern: for the EEPs shown in Figures 2 and 3, the Root Mean Square (RMS) value of the logarithmic difference (RMS discrepancy hereinafter) (computed for each element across the zenith angle, about 400 samples) has been reduced from an average value between the elements of 0.6 dB (original) to 0.4 dB (after time-shift correction). The ripple reduction is associated to the improved effectiveness of the compensation for the UAV variable attitude during the flight [18].

Figures 4 and 5 show the synoptic visualization for AAVS1.5 and EDA2, respectively. It contains both the agreement between measured and simulated EEP and the active-element gain for all the elements at all frequencies. Each cluster/frequency is arranged in a different row/column.

In order to allow for a direct comparison of the agreement between measurements and simulations

regardless of the level (which depends on the receiver gain), each measured EEP has been equalized to the corresponding simulated curve. In particular, a constant gain, G_n, is added to the measured EEPs to minimize the RMS discrepancy. The obtained RMS discrepancy of each element is shown with cyan/magenta dots. Larger values are concentrated at 50 MHz and 160 MHz for AAVS1.5, and at 320 MHz for EDA2. The magenta dots of some elements of EDA2 at 70 MHz indicate that the Low Noise Amplifier (LNA) at the antenna level was close to the saturation point. The clipped signal caused a distortion in the measured pattern; however, the final RMS is still comparable to the other elements.

The bars report instead the measured relative active element gain distribution. Element #8 of cluster #2 and element #2 of cluster #2 have been adopted as gain-reference antennas for AAVS1.5 and EDA2, respectively, in order to focus the analysis on the relative differences between the array elements. Letting G_{ref} be the normalization constant of the reference element, the bars represent the quantity ($G_{ref} - G_n$). The low gain level of element #14 of AAVS1.5 (black bar) highlights a damage in the optical link between the LNA and the receiver that caused a high signal loss. Other elements show a considerably low gain (e.g. EDA2, #10 of cluster #0 and #15 of cluster #1), which reduces the signal-to-noise ratio increasing the RMS discrepancy.

For the chosen reference antennas, the absolute gain level has been measured according to the procedure described in [14], i.e. a reference measurement of the UAV generator directly connected to the input of the receiver chain (input of the *smartbox*, i.e. where the element cables are collected) is exploited in order to calibrate out several error contributions such as transmitted power and receiver gain. Tables 1 and 2 report both the measured and simulated gain values at different frequencies (isolated antenna plus LNA). According to the error estimation of [19], the mismatched UAV dipole can explain discrepancies at 50 MHz. The error for the gain-reference element of AAVS1.5 generally decreases at higher frequencies, whereas the EDA2 reference antenna shows a more variable discrepancy. The latter can be improved with a further refinement of the considered models with particular reference to the interaction between LNA and antenna (transducer gain) in the embedded conditions.

Finally, Figures 6 and 7 show the normalized beam-formed pattern of cluster #0 (16 antennas) of AAVS1.5 and EDA2, respectively. As expected, the results are rather similar to each other, even though some elements present different behavior. The measured array pattern (blue) has been obtained by equalizing the complex EEPs at the zenith of the cluster. This corresponds to a near-field focusing, i.e a quadratic phasing of the array elements. The simulations (red) are

instead performed in far-field using the Method of Moments (MoM) of Galileo-EMT. The good agreement confirms the accuracy of the array model, as well as the effectiveness of the near-field focusing concept for large-array testing [20], [21].

TABLE I: MEASURED AND SIMULATED ACTIVE-ELEMENT GAIN AT ZENITH FOR THE CHOSEN GAIN-REFERENCE ANTENNA OF AAVS1.5.

Frequency (MHz)	Measured gain (dBi)	Simulated gain (dBi)	Discrepancy (dB)
50	34.29	36.47	-2.18
70	46.69	48.80	-2.11
110	52.52	51.90	+0.62
160	51.58	52.24	-0.66
320	50.50	49.92	+0.58

TABLE II: MEASURED AND SIMULATED ACTIVE-ELEMENT GAIN AT ZENITH FOR THE CHOSEN GAIN-REFERENCE ANTENNA OF EDA2.

Frequency (MHz)	Measured gain (dBi)	Simulated gain (dBi)	Discrepancy (dB)
50	-3.81	-1.99	-1.82
70	17.04	14.48	+2.57
110	19.94	18.88	+1.06
160	26.23	26.30	-0.07
320	20.44	24.06	+3.61

4. Conclusion

This first measurement campaign in Western Australia using a UAV-mounted test source has been conceived to support the deployment the SKA-low prototypes and verify the array models. The presented synoptic visualization concentrates a large amount of data collected within a limited number of flights, highlighting the benefit of using a UAV-mounted test source for array characterization and operative verification. Further activities will concern the whole 256-elements stations both in terms of the pattern characterization (also adopting near-field strategies) and the evaluation of the instrument performance (e.g. sensitivity).

5. Acknowledgement

6. References

1. P. E. Dewdney, P. J. Hall, R. T. Schilizzi, and T. J. L. W. Lazio, "The Square Kilometre Array," *Proceedings of the IEEE*, **97**, 8, Aug. 2009, pp. 1482-1496.

2. P. Benthem et al., "The low frequency receivers for SKA 1-low: Design and verification," XXXIInd General Assembly and Scientific Symposium of the International Union of Radio Science (URSI GASS), 2017, Montreal, QC.

3. P. Di Ninni, M. Bercigli, P. Bolli, G. Virone, and S. J. Wijnholds, "Mutual Coupling Analysis for a SKA1-LOW Station," 13th European Conference on Antennas and Propagation (EuCAP), 2019, Krakow, Poland.

4. R. Wayth et al., "The Engineering Development Array: A Low Frequency Radio Telescope Utilising SKA Precursor Technology," *Publications of the Astronomical Society of Australia*, **34**, E034, 2017.

5. S. Tingay et al., "The Murchison Widefield Array: The Square Kilometre Array Precursor at Low Radio Frequencies," *Publications of the Astronomical Society of Australia*, **30**, E007, 2013.

6. G. Virone et al., "Strong Mutual Coupling Effects on LOFAR: Modeling and In Situ Validation," *IEEE Transactions on Antennas and Propagation*, **66**, 5, May 2018, pp. 2581-2588.

7. P. Bolli et al., "In-situ characterization of international low-frequency aperture arrays by means of an UAV-based system," XXXII General Assembly and Scientific Symposium of the International Union of Radio Science (URSI GASS), 2017, Montreal, QC.

8. E. de Lera Acedo et al., "SKA Aperture Array Verification System: Electromagnetic modeling and beam pattern measurements using a micro UAV", *Experimental Astronomy*, **45**, 1, Mar. 2018, pp. 1–20.

9. P. Di Ninni et al., "Electromagnetic analysis and experimental validation of the LOFAR radiation patterns," *International Journal of Antennas and Propagation*, 9191580, 2019.

10. P. Bolli, G. Pupillo, F. Paonessa, G. Virone, S. J. Wijnholds and A. M. Lingua, "Near-Field Experimental Verification of the EM Models for the LOFAR Radio Telescope," *IEEE Antennas and Wireless Propagation Letters*, **17**, 4, April 2018, pp. 613-616.

11. L. Ciorba et al., "Near-Field Phase Reconstruction for UAV-based Antenna Measurements," 13th European Conference on Antennas and Propagation (EuCAP), 2019, Krakow, Poland.

12. F. Paonessa et al., "First Results on the Experimental Validation of the SKA-low Prototypes Deployed in Australia

Using an Airborne Test Source," XXXIII General Assembly and Scientific Symposium of the International Union of Radio Science (URSI GASS), 2020, Rome, Italy.

13. D. B. Davidson et al., "Electromagnetic modelling of the SKA-LOW AAVS1.5 prototype," International Conference on Electromagnetics in Advanced Applications (ICEAA), 2019, Granada, Spain.

14. F. Paonessa et al., "Characterization of the Murchison Widefield Array Dipole with a UAV-mounted Test Source," 13th European Conference on Antennas and Propagation (EuCAP), 2019, Krakow, Poland.

15. F. Paonessa, G. Virone, P. Bolli, G. Addamo, S. Matteoli and O. A. Peverini, "UAV-Based Antenna Measurements: Improvement of the Test Source Frequency Behavior," IEEE Conference on Antenna Measurements & Applications (CAMA), 2018, Vasteras, Sweden.

16. F. Paonessa, G. Virone, P. Bolli and A. M. Lingua, "UAV-based antenna measurements: Scan strategies," 11th European Conference on Antennas and Propagation (EUCAP), 2017, Paris, France.

17. S. Pivnenko et al., "Comparison of Antenna Measurement Facilities With the DTU-ESA 12 GHz Validation Standard Antenna Within the EU Antenna Centre of Excellence," *IEEE Transactions on Antennas and Propagation*, **57**, 7, July 2009, pp. 1863-1878.

18. F. Paonessa et al., "Effect of the UAV orientation in antenna pattern measurements," 2015 9th European Conference on Antennas and Propagation (EuCAP), 2015, Lisbon, Portugal.

19. P. Bolli, F. Paonessa, G. Pupillo, G. Virone, M. Arts, A. Lingua, J. Monari, S. J. Wijnholds, "Antenna pattern characterization of the low-frequency receptor of LOFAR by means of an UAV-mounted artificial test source," Proc. SPIE 9906, Ground-based and Airborne Telescopes VI, 99063V, 2016, Edinburgh, United Kingdom.

20. P. Nepa and A. Buffi, "Near-Field-Focused Microwave Antennas: Near-field shaping and implementation.," *IEEE Antennas and Propagation Magazine*, **59**, 3, June 2017, pp. 42-53.

21. J. Sherman, "Properties of focused apertures in the Fresnel region," *IRE Transactions on Antennas and Propagation*, **10**, 4, July 1962, pp. 399-408.

F. Paonessa, L. Ciorba and G. Virone are with Italian National Research Council (CNR), Institute of Electronics, Computer and Telecommunication Engineering (IEIIT), Corso Duca degli Abruzzi, 24, 10129 Turin, Italy; e-mail: fabio.paonessa@ieiit.cnr.it; lorenzo.ciorba@ieiit.cnr.it; giuseppe.virone@ieiit.cnr.it.
P. Bolli is with Italian National Institute for Astrophysics (INAF), Arcetri Astrophysical Observatory (OAA), Largo Enrico Fermi, 5, 50125 Florence, Italy. e-mail: pbolli@arcetri.inaf.it.

A. Magro is with Institute of Space Sciences and Astronomy, University of Malta, Msida, MSD2080, Malta. e-mail: alessio.magro@um.edu.mt.
A. McPhail, D. Minchin and R. Bhushan are with International Centre for Radio Astronomy Research (ICRAR), 1 Turner Avenue, Bentley, Western Australia, 6102. e-mails: andrew.mcphail@icrar.org; dave.minchin@icrar.org; raunaq.bhushan@icrar.org.
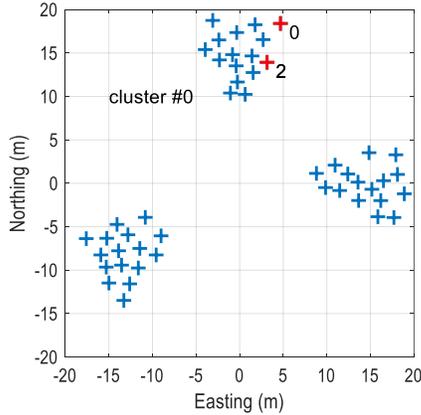
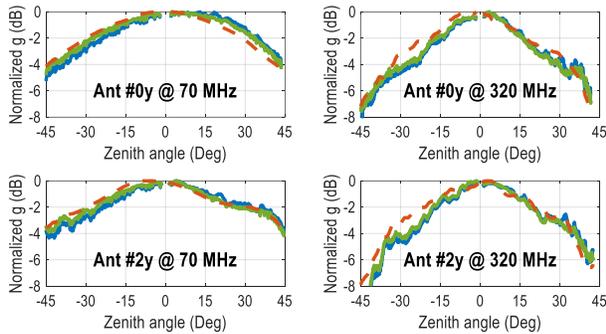Figure 1. Layout of AAVS1.5. Antennas #0 and #2 of cluster #0 highlighted.

Figure 2. Normalized embedded-element patterns of antenna #0 (upper row) and #2 (lower row) of AAVS1.5 (north-south polarization, cluster #0) at 70 MHz (left column) and 320 MHz (right column). Blue: original measurements, green: measurements with time-shift correction applied, red: simulations.
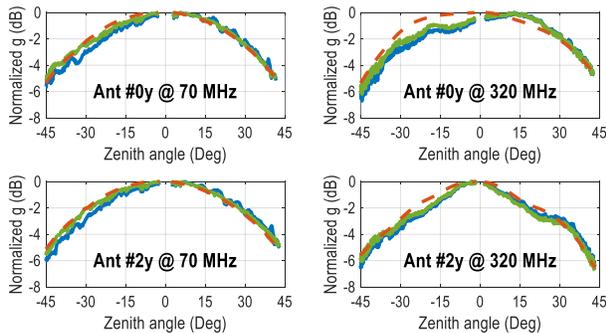

Figure 3. Normalized embedded-element patterns of antenna #0 (upper row) and #2 (lower row) of EDA2

(north-south polarization, cluster #0) at 70 MHz (left column) and 320 MHz (right column). Blue: original measurements, green: measurements with time-shift correction applied, red: simulations.
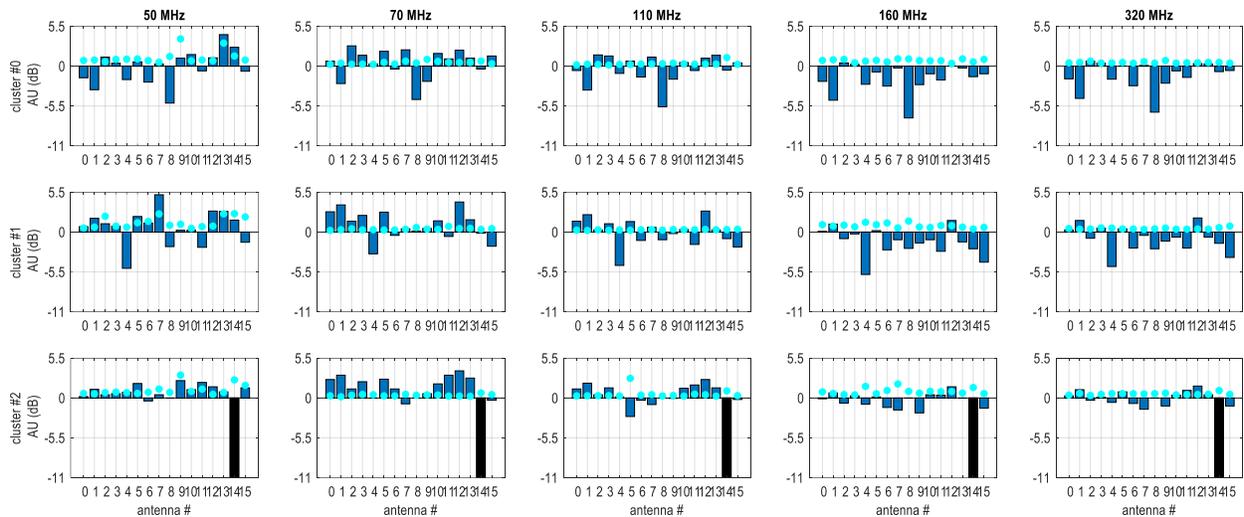
Figure 4. Synoptic visualization of the AAVS1.5 results. Clusters from #0 to #2 in each row. Frequencies from 50 MHz to 320 MHz in each column. Dots: RMS discrepancy between measured and simulated EEP. Bars: measured relative active-element gain. The actual value of the black bar is out of range (damaged wired link).
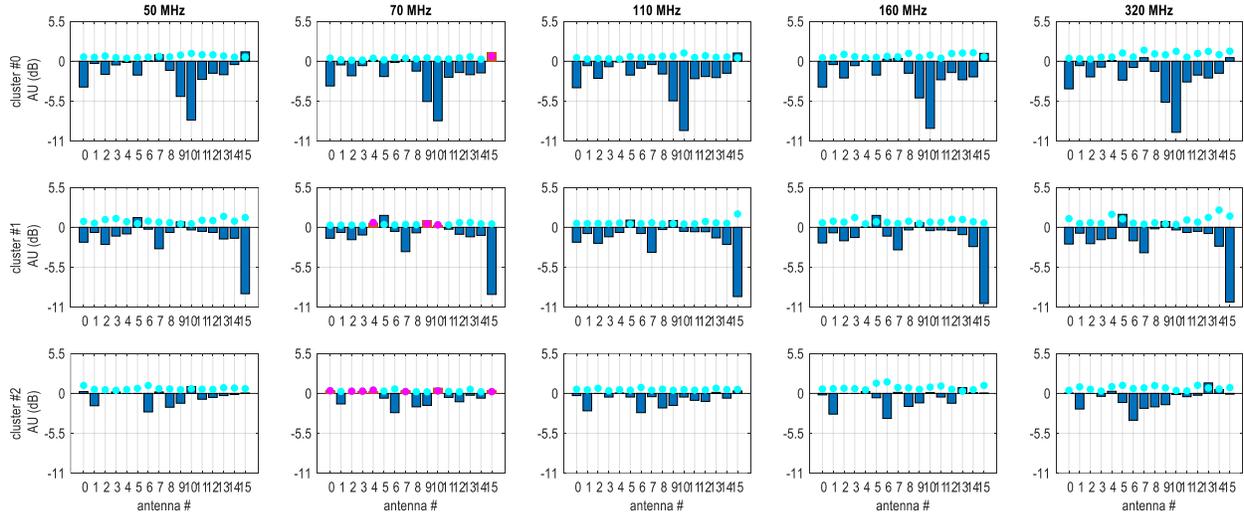

Figure 5. Synoptic visualization of the EDA2 results. Clusters from #0 to #2 in each row. Frequencies from 50 MHz to 320 MHz in each column. Dots: RMS discrepancy between measured and simulated EEP. Bars: measured relative active-element gain.
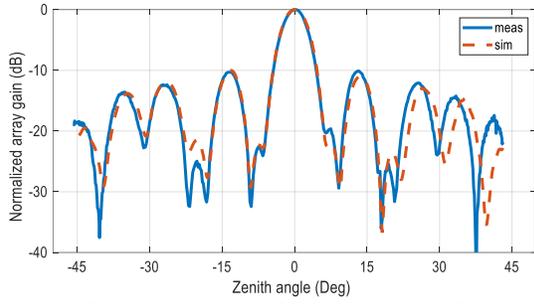
Figure 6. Normalized beam-formed pattern of cluster #0 of AAVS1.5 at 320 MHz. Blue: measurements, red: simulations.
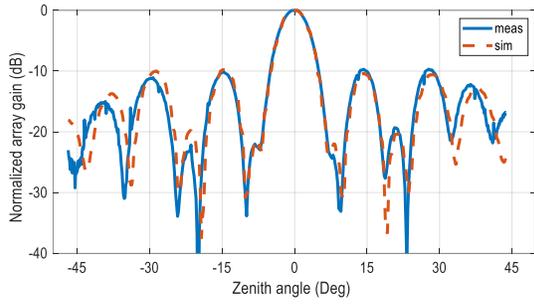

Figure 7. Normalized beam-formed pattern of cluster #0 of EDA2 at 320 MHz. Blue: measurements, red: simulations.